

See discussions, stats, and author profiles for this publication at: <https://www.researchgate.net/publication/376563536>

Benefit of incorporating GLASS remote sensing vegetation products in improving Noah-MP land surface temperature simulations on the Tibetan Plateau

Article in *Science of Remote Sensing* · December 2023

DOI: 10.1016/j.srs.2023.100115

CITATIONS

0

5 authors, including:



Qing He

The University of Tokyo

13 PUBLICATIONS 82 CITATIONS

[SEE PROFILE](#)

READS

63



Hui Lu

Tsinghua University

242 PUBLICATIONS 6,247 CITATIONS

[SEE PROFILE](#)



Kun Yang

Tsinghua University

327 PUBLICATIONS 19,720 CITATIONS

[SEE PROFILE](#)

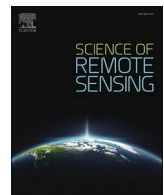
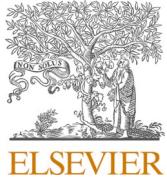


Long Zhao

Southwest University in Chongqing

64 PUBLICATIONS 2,086 CITATIONS

[SEE PROFILE](#)



Benefit of incorporating GLASS remote sensing vegetation products in improving Noah-MP land surface temperature simulations on the Tibetan Plateau

Qing He ^{a,b,*}, Hui Lu ^{b,f,g,**}, Kun Yang ^{b,c}, Long Zhao ^d, Mijun Zou ^e

^a River and Environmental Engineering Laboratory, The University of Tokyo, Tokyo, Japan

^b Department of Earth System Science, Tsinghua University, Beijing, China

^c Tibetan Plateau Data Center, State Key Laboratory of Tibetan Plateau Earth System and Resource Environment, Institute of Tibetan Plateau Research, Chinese Academy of Sciences, Beijing, China

^d School of Geographical Sciences, Southwest University, Chongqing, China

^e School of Environmental and Geographical Sciences, Shanghai Normal University, Shanghai, China

^f Tsinghua University (Department of Earth System Science), Xi'an Institute of Surveying and Mapping Joint Research Center for Next-Generation Smart Mapping, Beijing, China

^g State Key Laboratory of Hydroscience and Engineering, Tsinghua University, Beijing 100084, China

ARTICLE INFO

Keywords:

Land surface temperature

Leaf area index

Fraction of vegetation cover

Land surface models

ABSTRACT

Land Surface Temperature (LST) is important for diagnosing surface energy balance in land surface models (LSMs). However, LST simulation in current LSMs tends to show large cold biases, partially due to the reason that the model's prescribed vegetation parameters (e.g., Leaf Area Index (LAI) and Fraction of Vegetation Cover (FVC)) are misrepresented, especially in regions with complex topography and climate such as Tibetan Plateau. Recent advancements in remote sensing technologies provide a unique opportunity to improve the model's vegetation parameters at large scales. In this study, we practice two experiments to improve LST simulations in Noah-MP LSM by (1) incorporating LAI and FVC from the Global Land Surface Satellite (GLASS) remote sensing product (exp_RS); and (2) incorporating an empirical LAI and FVC parameterization scheme based on the soil temperature stress factor (exp_RL02). Results show that the effect of vegetation on simulated LST is the most significant in summer season when the model-satellite LAI and FVC differences are the largest. Compared to the default experiment that uses static LAI and FVC values from the model's look-up table (exp_CTL), the results in exp_RS and exp_RL02 show domain-wide improvement of the simulated LST. The LAI and FVC effect on LST are also well reflected in model's energy budget components (i.e., longwave emissivity, sensible and latent heat fluxes, etc). Validation of the model simulated soil temperature with in-situ observations further demonstrate the model improvements. Our study underscores the important role of vegetation in regulating surface energy transfer processes. Our study also highlights the feasibility and benefit of incorporating remote sensing data in improving land surface model simulations.

1. Introduction

Land surface temperature (LST) is an important diagnosis to examine surface energy balance in Land Surface Models (LSMs) (Chen et al., 2011; Li et al., 2019). However, accurately simulating LST has been challenging since the physical processes between land and atmosphere are complex and many of them are often tightly coupled (Seneviratne et al., 2010). Previous studies (Wang et al., 2014; Yang et al., 2009,

2011) have reported substantial LST biases in several major LSMs, including the Simple Biosphere Model version 2 (Sellers et al., 1996), Community Land Model version 4 (Lawrence et al., 2011), and Noah Land Surface Model with Multiple Parameterizations (Noah-MP, Niu et al., 2011). In these studies, the models tend to show large cold biases over areas with complex topography, for example, the Midwest U.S. and the Tibetan Plateau. The cold biases may be caused by the model's overestimation of the cooling effect associated with lapse rate and

* Corresponding author. River and Environmental Engineering Laboratory, The University of Tokyo, Tokyo, Japan.

** Corresponding author. Department of Earth System Science, Tsinghua University, Beijing, China.

E-mail addresses: heqing@g.ecc.u-tokyo.ac.jp (Q. He), luhui@tsinghua.edu.cn (H. Lu).

orographic precipitation (Gao et al., 2015), which are determined by land-atmosphere heat exchanges that are relevant to land cover properties. As such, appropriate characterization of key land surface parameters over these areas could effectively help reduce the cold bias of LST simulation in current LSMs.

One of the core land surface parameters that control land surface energy balance lies in vegetation characteristics. The vegetation growth can increase evapotranspiration (ET), leading to changes in surface heat fluxes, and thus lowering the boundary layer height and development of convective precipitation (Gentine et al., 2011, 2013). Meanwhile, vegetation canopy reflects the surface incoming solar radiation as well as the longwave fluxes emitted by the ground, while the penetrated fluxes are again reflected and scattered by plant leaves, causing redistribution of surface radiation fluxes over the vegetated areas (Dickinson, 1983; Sellers, 1985; Yang and Niu, 2003). In the above processes, two parameters play key roles: the Fraction of Vegetation Cover (FVC) determines how much radiation fluxes are reflected by the vegetation canopy; and the Leaf Area Index (LAI) determines how much radiation can be penetrated through the canopy and how are the fluxes redistributed by plant leaves.

The original two major approaches to represent LAI and FVC in current LSMs are: (1) Using a prescribed Look-Up Table (LUT) where LAI and FVC are fixed for each vegetation type; and (2) Using parameterization schemes that are empirically based on field experiments at the point scale. However, the largest shortcoming is that, the LAI and FVC distribution in the real world are largely affected by vegetation characteristics (e.g., canopy shapes and tilting angles of the leaves) that are uniquely dependent on plant species (Chen et al., 2003; Roujean, 1996). Such a situation is quite significant on Tibetan Plateau, for example, compared to other species under the same vegetation classification category, the plant canopy is more clumped due to adaptation to coldness (e.g., Ni, 2000), therefore less radiation reflected back from the land surface, and finally, the warmer surface temperature if all other conditions were equal. Applying the general classification of vegetation types to studies on Tibetan Plateau may not be able to specify the distinctive vegetation properties therein, and therefore may lead to cold-biased land surface energy balance simulation. Furthermore, for the parameterization approach, the LAI and FVC calculation schemes implemented in current models are sometimes too simple to include the key limiting factors on vegetation growth (e.g., soil temperature or water stress on vegetation growth (Dai et al., 2003; Ji and Dai, 2010)), therefore tend to overestimate the vegetation coverage and colder land surface temperature simulations (Li et al., 2019; Nogueira et al., 2020).

Recently, owing to the advancement of remote sensing technologies, the third approach, i.e., incorporating the real-time satellite LAI and FVC images, has been introduced to improve LST simulations. Indeed, satellite observations can provide more realistic LAI and FVC distribution compared to LUT- and parameterization-based approaches. There are already studies showing significant improvements in models' performance on simulating LST on Carbon-Hydrology Tiled ECMWF Scheme for Surface Exchanges over Land (CHTESSEL) model (Nogueira et al., 2020) and Common Land Model (CoLM) (Li et al., 2019) by using the remote sensing-based approach. However, such a method is rarely practiced in the LSMs that were previously reported to show large LST cold biases (i.e., SiB2, CLM, and Noah-MP). Meanwhile, the above studies also show that how much LST can be improved is largely model-dependent, for example, the LST improvement is more significant in CoLM since the original LAI and FVC values are more fixed in CoLM, e.g., LAI LUT in CoLM does not have seasonal variations, and the FVC is prescribed as a binary variable at each grid cell. Therefore, it is necessary to leverage the benefit of the remote sensing-based approach to improve LST simulation in LSMs that are subject to large LST cold biases.

In this study, we aim to demonstrate the benefit of incorporating remote sensing LAI and FVC products in LST simulations in a state-of-art land surface model (i.e., Noah-MP) (Niu et al., 2011; Yang et al., 2011). The Tibetan Plateau is chosen as the study region because it plays a

crucial role in regulating regional climate due to its unique geographical characteristics, while the LST simulations in this region are usually subject to large cold biases. Noah-MP model is chosen here because the model has been extensively evaluated and many land surface parameters (excluding LAI and FVC) such as soil organic matter content and surface roughness are well calibrated on the Tibetan Plateau (Zheng et al., 2015; Sun et al., 2021, 2022), providing a valid testbed for further improving its LST simulation from remote sensing vegetation products. Moreover, it is also one of the major land surface models that have already been coupled to the regional weather forecast model WRF (Weather Research and Forecast) (Barlage et al., 2015; García-García et al., 2020; Tian et al., 2020), so that the improvement on the land surface in this study can be conveniently transferred to the atmospheric simulations by further efforts.

Two experiments are conducted in this study: (1) incorporating the real-time satellite images of LAI and FVC to replace the model's prescribed LUT; and (2) an empirical FVC scheme that considers the environmental limitations (e.g., soil temperature) in controlling vegetation growth is also implemented to demonstrate to what extent the remote sensing products can help improve model as compared to the traditional parameterization-based method. To validate the results, LST observations retrieved from the satellite and the soil temperature from in-situ observations are used to compare with the model simulations. Our study provides a satellite-based reference for improving LST simulations in Noah-MP, highlighting the important roles of vegetation in controlling the models' energy exchanges between land and near-surface atmosphere.

2. Data and methods

2.1. Methods

Noah-MP LSM (Niu et al., 2011; Yang et al., 2011) includes the key hydrometeorological and biophysical processes such as soil freeze-thawing, water flux exchanges at the stomatal level, and carbon accumulation of plant leaves, etc. Multiple parameterization options are available for each process, making the performance of Noah-MP simulations superior to other major LSMs (Cai et al., 2014a, 2014b). The Noah-MP model has been evaluated at different regions and spatial scales (Liang et al., 2019; Ma et al., 2017; Niu et al., 2011; Yang et al., 2011). However, studies on Tibetan Plateau are comparatively few due to the scarce availability of land surface observations, especially in terms of the model's LST improvement.

In Noah-MP LSM, a subgrid scheme is used to split an entire grid into two parts: a fractional vegetation area (FVC) and a fractional area covered by bare soil ($1 - FVC$). The surface radiation fluxes are calculated through the modified two-stream scheme as a function of LAI and FVC. LST is then calculated as a combined function of surface radiation fluxes over the vegetated area and the bare soils. One option to calculate LAI in Noah-MP is to use the monthly mean values from LUT, which are extracted from the MODerate-resolution Imaging Spectroradiometer (MODIS) 2006 product and further classified based on United States Geological Surveys (USGS) vegetation types. As aforementioned, using the static monthly-mean LUT cannot reflect the sub-monthly variations of land surface reflectance properties dominated by vegetation cover, therefore may cause biases in the model's energy balance simulation.

The other option in Noah-MP is to calculate FVC as a function of LAI and Stem Area Index (SAI) (Equation (1)), with α for the combined effects of leaf albedo, leaf projection factor and vegetation structure. Therefore, α should be varying across biomes since the factors mentioned above depends largely on vegetation types, for example, the canopy shapes in boreal and tropical forests are quite different from those of mid-latitude crop and grasslands. However, in Noah-MP this parameter is constantly set to 0.52 for any vegetation type for the simplicity of the model structure.

Table 1
Three experiments settings in this study.

LAI	FVC	Model configuration	Other physical schemes
CTL	LUT	Eq (1)	Period:
RS	GLASS	GLASS	2010.01.01–2013.12.31
RL02	Eq (2)	Eq (4)	Time step: half hourly Spatial resolution: 0.1°

Stomatal resistance = Jarvis (Jarvis, 1976);
Soil moisture stress factor = CLM; Runoff = TOPMODEL with groundwater();
Surface drag = Monin-Obuhov;
Radiative transfer = Two-stream (Yang and Friedl, 2003);
Snow albedo = CLASS (Verseghy, 1991);
Surface resistance = (Sakaguchi and Zeng, 2009)

$$FVC = 1 - e^{-\alpha(LAI+SAI)} \quad (1)$$

where, FVC is the fraction of vegetation cover area (unitless); LAI and SAI denotes leaf area index (unitless) and stem leaf area index (unitless) and are both prescribed as multi-year monthly values in the look-up table.

To mend the above issues, three model runs are performed to improve LST simulation in Noah-MP and evaluate the vegetation effects on the model's energy balance (Table 1). The reference run (CTL) uses LAI from the model's LUT and the FVC is calculated from Equation (1). Experiment RS is conducted to incorporate real-time observations of LAI and FVC from the Global Land Surface Satellite (GLASS) dataset (see section 2.2 for data description). The model is forced with China Meteorological Forcing Dataset (CMFD) and is run at a half-hourly time step. The simulation period is from UTC0000, January 1st, 2008 to UTC2300, December 31, 2010. We take the first two-year simulation as the spin-up time while using the simulation from the last year for the main analyses in this study. Other physical schemes including canopy stomatal resistance, surface radiative transfer, etc. Are denoted in Table 1.

An additional experiment RL02 is designed to simulate LAI using an empirical scheme considering soil temperature effects on plant growth, which has been implemented in the Common Land Model (CoLM) and proved to show good performance (Dai et al., 2003; Ji and Dai, 2010). The scheme can be described as:

$$LAI = LAI_{min} + (LAI_{max} - LAI_{min}) \bullet (1 - f) \quad (2)$$

where, LAI_{min} and LAI_{max} represent the minimum and maximum LAI data for different vegetation types respectively, which was collected from a large number of ground sites worldwide that cover a variety of climate and biomes (Scurlock et al., 2002). The parameter f represents the soil temperature effects on vegetation growth and can be calculated as an empirical function of ST at soil layers where the accumulated root fraction reaches above 90%:

$$f = \max \left\{ \frac{0}{1 - 0.0016 \bullet \left(\max \left\{ \begin{array}{l} 298 - ST(Nroot) \\ 0 \end{array} \right\} \right)^2} \right\} \quad (3)$$

where, $Nroot$ is the soil layer where the accumulated root fraction reaches above 90%. The FVC in experiment RL02 is calculated from a revised FVC scheme from Roujean and Lacaze (2002):

$$FVC = 1 - e^{-b \frac{G(\theta_s)}{\cos \theta_s} \bullet \Omega \bullet LAI} \quad (4)$$

where, $b = 0.5$ indicates the leaf albedo effects, $G(\theta_s) = 0.945$ indicates

the leaf projection, and the solar zenith angle θ_s is set to 0 as in Roujean and Lacaze (2002). Ω refers to the clumping index (CI) and is retrieved from the satellite observations. LAI is calculated from Equation (2).

2.2. Datasets

The first high spatial-temporal resolution gridded near-surface meteorological dataset China Meteorological Forcing Dataset (CMFD) is used as the forcing data to drive Noah-MP model in this study (He et al., 2020). Combined several global fine-quality meteorological products with nearly 700 in-situ observations from the China Meteorological Administration (CMA) weather stations and incorporating a hybrid interpolating model with attenuated processing errors, CMFD provides a higher-resolution meteorological forcing dataset with good data quality that is more suitable for terrestrial modeling in mainland China compared to other widely-used global datasets (Chen et al., 2011; Liu and Xie, 2013; Tian et al., 2020; Yang et al., 2017, 2020), particularly in areas with complex topography such as Tibetan Plateau (Guo and Wang, 2013; Kang et al., 2022; Li et al., 2019, 2020; Wang et al., 2020). CMFD provides seven near-surface meteorological variables (i.e., 2-m air temperature, surface pressure, surface specific humidity, 10-m windspeed, downward shortwave radiation, downward longwave radiation and precipitation rate) from January 1979 to the present. The CMFD dataset has a temporal resolution of 3 h and a spatial resolution of 0.1° and can be accessed at <https://poles.tcdc.ac.cn/en/data/8028b944-daaa-4511-8769-965612652c49/>.

GLASS LAI and FVC products (Xiao et al., 2014, 2016a) are used to incorporate with Noah-MP model in this study (data available at <http://www.geodata.cn>). The temporal resolution of GLASS LAI and FVC product is 8 days and the spatial resolution is originally at 0.05deg. The GLASS LAI and FVC products provide long-term global vegetation maps generated from Advanced Very High Resolution Radiometer (AVHRR) and MODIS and are proved to have superior temporal smoothness and closer mean values to field experiments (e.g., BigFoot projects reported in Garrigues et al., 2008; Camacho et al., 2013), and is temporally more continuous compared to several existing LAI and FVC products (Xiao et al., 2016b). The availability of long-term, global scale GLASS LAI and FVC product has facilitated many studies relevant to surface water and carbon estimates (Liu et al., 2018) and model development (Kumar et al., 2019). Furthermore, we use a global 500 m clumping index (CI) dataset (available at https://daac.ornl.gov/VEGETATION/guides/Global_Clumping_Index.html; He et al., 2012) as the input for the empirical vegetation scheme (see Section 2.2 below). The CI data is provided with only a single year of 2006. However, its inter-annual variations are shown to be limited over most land cover types on the Tibetan Plateau (e.g., standard deviation < 0.1) (Jiao et al., 2018; Zhu, 2016; Zhu et al., 2012). It is as such reasonable to use one-year data to characterize the overall CI characteristics.

LST products from MODIS MYD11C1 (<https://lpdaac.usgs.gov/products/myd11c1v006/>) products are used to evaluate LST simulations in the conducted analyses. MYD11C1 product is chosen here since it is retrieved from the Aqua satellite, which has an overpass time around 1:30 p.m. (local solar time) in its ascending mode. This may present a more indicative comparison between the LSMs and the satellite observation because at noontime the LSMs tend to misestimate LST most remarkably when LST is reaching its peak during its diel variations (Chen et al., 2011; Li et al., 2019; Yang et al., 2009). The MYD11C1 LST product was filtered to limit the effects of potential error sources, such as coverage of clouds (and nearby clouds), missing pixels, retrieving methods and calibration errors (Wan, 2013). Additionally, MODIS MCD43C3 Version 6 Bidirectional Reflectance Distribution Function and Albedo (BRDF/Albedo) product (<https://lpdaac.usgs.gov/products/mcd43c3v006/>) is also used to evaluate the model's albedo simulations. MCD43C3 provides black-sky albedo and white-sky albedo at the visible (VIS), near infrared (NIR), and shortwave bands, respectively. Here we use the average black-sky albedo of VIS and NIR in the main

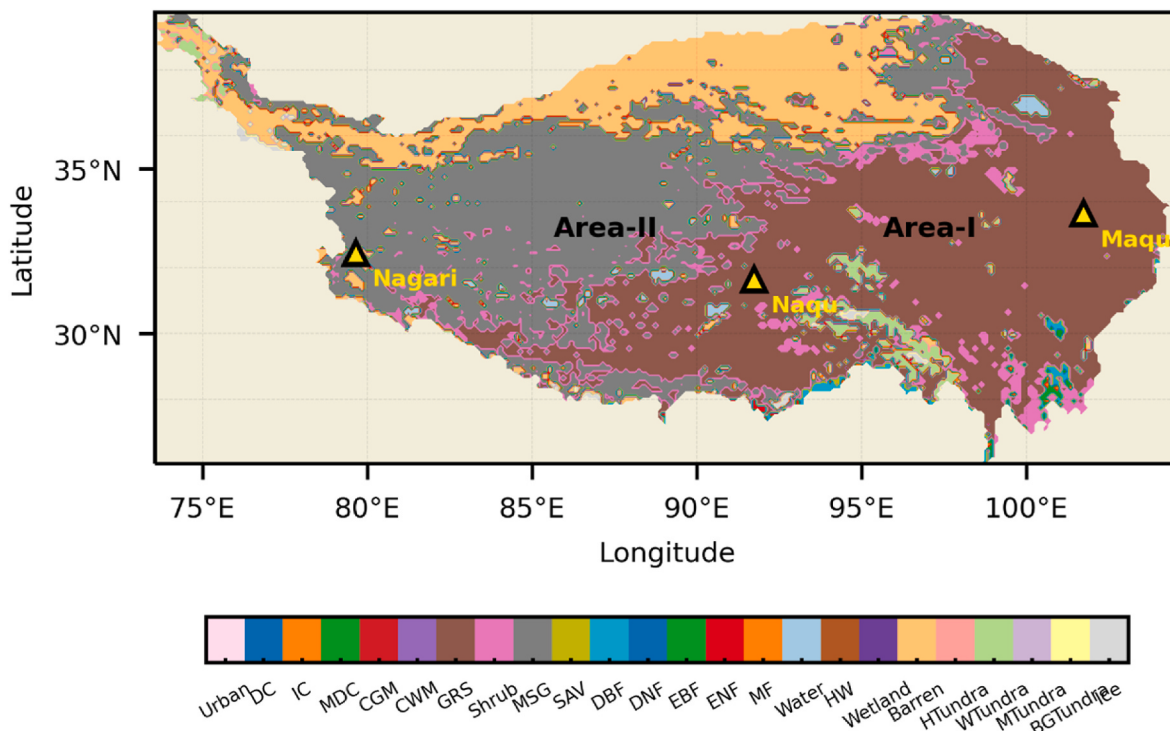


Fig. 1. Prescribed land cover types on Tibetan Plateau in Noah-MP LSM and geographical locations of the three soil temperature observing networks. Full names of the land cover types are: Urban = Urban and Built-Up Land; DC = Dryland Cropland; IC = Irrigated Cropland; MDC = Mixed Dryland/Irrigated Cropland; CGM = Cropland/Grassland Mosaic; CWM = Cropland/Woodland Mosaic; GRS = Grassland; Shrub = Shrubland; MSG = Mixed Shrubland and Grassland; SAV = Savanna; DBF = Deciduous Broadleaf Forest; DNF = Deciduous Needleleaf Forest; EBF = Evergreen Broadleaf Forest; ENF = Evergreen Needleleaf Forest; MF = Mixed Forest; Water = Water Bodies; HW = Herbaceous Wetland; HTundra = Herbaceous Tundra; WTundra = Wooded Tundra; MTundra = Mixed Tundra; BGTundra = Bare Ground Tundra. As indicated above, the two primary vegetation types on Tibetan Plateau in Noah-MP are Mixed Shrublands/Grasslands (Dark Gray, Area-I) and Grasslands (Dark Brown, Area-II). Therefore, some of the model simulation results are analyzed based on the two main subregions. (For interpretation of the references to color in this figure legend, the reader is referred to the Web version of this article.)

Table 2
Summary of the three soil temperature observing networks from Tibet-Obs.

	Geographical range	Number of Sites	Climate	Vegetation Density
Nagari	32.42–33.45 °N, 79.62–80.18 °E	20	Cold, arid	Sparse
Naqu	31.32–31.32 °N, 91.82–91.92 °E	5	Cold, semi-arid	Moderate
Maqu	33.09–34.02 °N, 101.72–102.57 °E	20	Cold, humid	Dense

context while retaining white-sky VIS/NIR-average to serve as a supplementary comparison. All the data described above are reprocessed to the spatial resolution of 0.1° using linear interpolation, in order to be consistent with the model's configuration. In addition, the model's output is also processed to be consistent with the satellite overpass time at each grid by using a similar algorithm as in a previous study (Li et al., 2019).

Finally, in-situ measurements of soil temperature are used to validate the model's simulation results. We use soil temperature here because there are no readily available LST field observations. Three in-situ observing networks of soil temperature including Nagari, Naqu, and Maqu from Tibet-Obs (Su et al., 2011) are used here. The observations are available at four soil layer depths (i.e., 5 cm, 10 cm, 20 cm, and 40 cm). However, we compare only the surface soil layer (i.e., 5 cm) since it corresponds more reasonably to LST variability. Therefore, only the 5 cm in-situ observations are used for evaluation. The surface soil layer depth in the Noah-MP simulation is set to 10 cm to ensure consistent soil layer depth between in-situ measurements and the model's

configurations. Locations of the three networks are illustrated as triangles in Fig. 1. At each observing network, soil temperature measurements are averaged from all individual stations to compare with the model simulations at grids of the same geographical range. Additionally, the geographical range, number of stations, climate type and vegetation coverage density of each observing network are summarized in Table 2. For detailed information of specific stations within each network, the readers are referred to (Su et al., 2011).

3. Results and discussion

3.1. Seasonal-dependent impact of satellite observations on model simulations

Since the vegetation-covered area and leaf density vary in different seasons, we first conducted intercomparisons of LUT-based and GLASS LAI and FVC products. From Fig. S1 we observe that although biases between LUT-based and GLASS LAI generally exist throughout the year (e.g., mean biases of LAI are 0.31, 1.36, 0.48 and 0.33 in March-April-May (MAM), June-July-August (JJA), September-October-November (SON), and December-January-February (DJF), respectively), the largest gap occurs in the summer season. Similar seasonal biases distribution is also observed in FVC, although the seasonality is less significant than LAI, where mean biases are 0.11 in spring and summer, while 0.07 in autumn and winter seasons (Fig. S2). The seasonal biases between LUT-based and GLASS products indicate that the vegetation's influence on land surface energy transfer processes may be the most substantial in summer.

To demonstrate the seasonal effect of vegetation on model simulation, we further compared the LST difference between exp_RS and

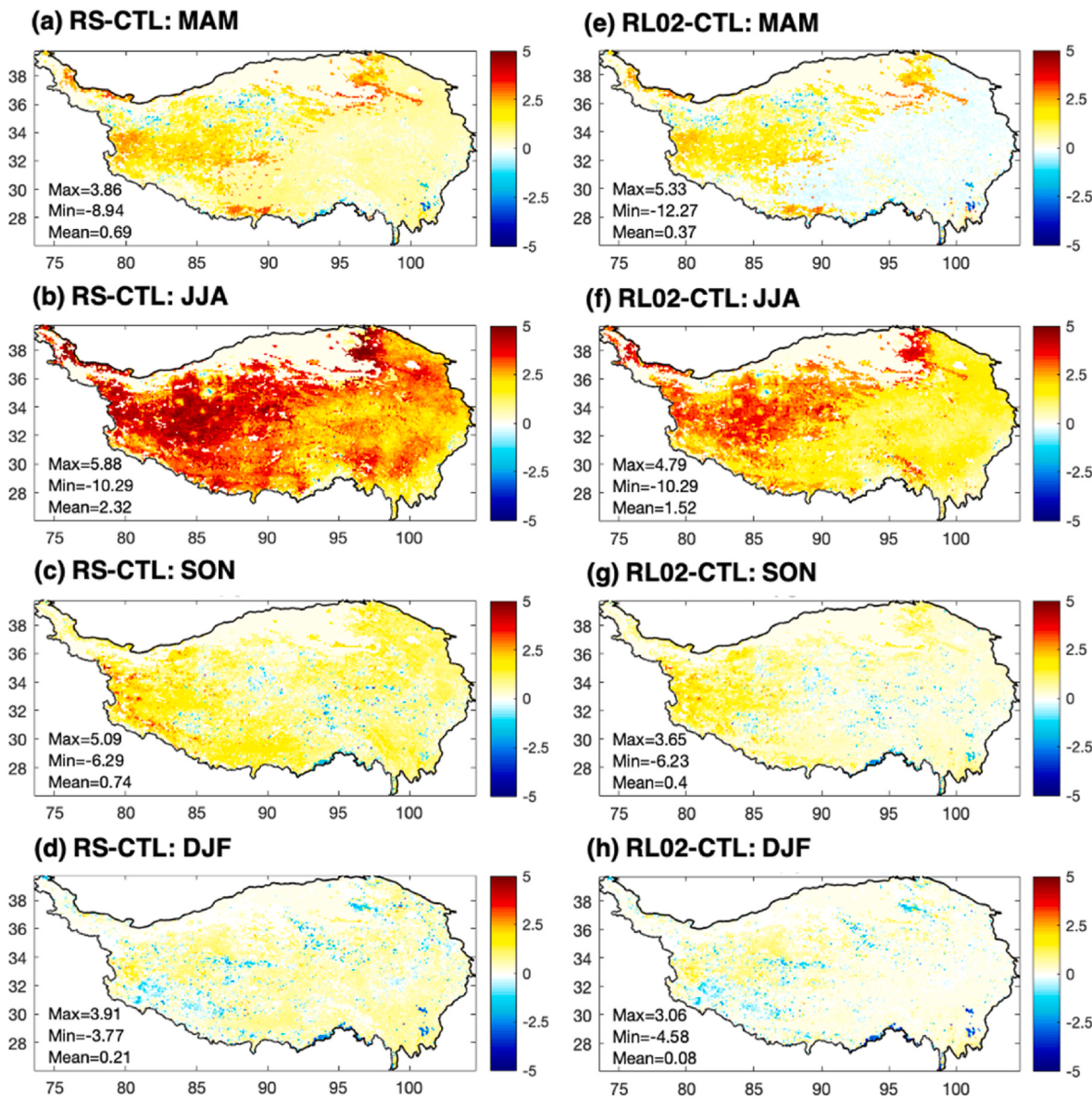


Fig. 2. Land Surface Temperature difference between exp_RS and exp_CTL (left column), and between exp_RL02 and exp_CTL (right column) for four seasons.

exp_CTL, and exp_RL02 and exp_CTL, respectively. Fig. 2 shows that the LST changes in other seasons are much less compared to summer (JJA). For example, the mean difference between exp_RS and exp_CTL is 2.3degC, with more than 50% areas showing larger than 2.5degC difference in summer; while in other seasons the mean difference are mostly less than 1 degC, and the majority of the study area showing LST difference less than 2.5degC. The seasonal characteristics in exp_RL02 – exp_CTL are much the same, except that the overall LST difference is less significant than the exp_RS – exp_CTL comparison. The above analyses suggest that the impact of LAI and FVC on model simulations are indeed the most observable in summer when the LUT-based and satellite observations disparities are the largest. In the following context, we will primarily focus on the analyses of summer season result.

3.2. Bias evaluation in the CTL experiment against satellite observations

Fig. 3 shows the spatial distribution of LAI and FVC results from experiment CTL as compared to GLASS products during June-July-August (JJA) season in the year 2010. The results show that the LUT-based LAI and FVC (Fig. 3a and c) show less spatial variability, while

the satellite-observed images (Fig. 3b and d) present a clear Southeast-Northwest gradient across Tibetan Plateau. By comparing with vegetation maps that were reported previously based on field observations, this result indicates the satellite-based LAI and FVC are more representative of the vegetation distribution (i.e., denser over the southeastern regions while sparse over western regions) on Tibetan Plateau. At the same time, the satellite-based LAI and FVC show much lower values over the entire domain in terms of magnitude, e.g., most of them are within the lowest 20 percentage (Fig. 3b and d, insets), indicating the LUT-based LAI and FVC are overestimated in Noah-MP LSM.

The overestimation of LAI and FVC from LUT may lead to bias in the model's energy balance transfer simulations. Therefore, in Fig. 3 we show the simulated albedo and LST results from the CTL experiment. Albedo from satellite observation (Fig. 4a) shows similar Southeast-Northwest gradients as those of LAI and FVC, with larger values in the less vegetated northwestern part. The probability density is unimodally distributed with the peak located at 0.15 (Fig. 4a, inset). The albedo result from CTL experiment also shows the Southeast-Northwest spatial gradient. However, the spatial pattern is noticeably opposite compared to the satellite observations, for example, the CTL experiment presents

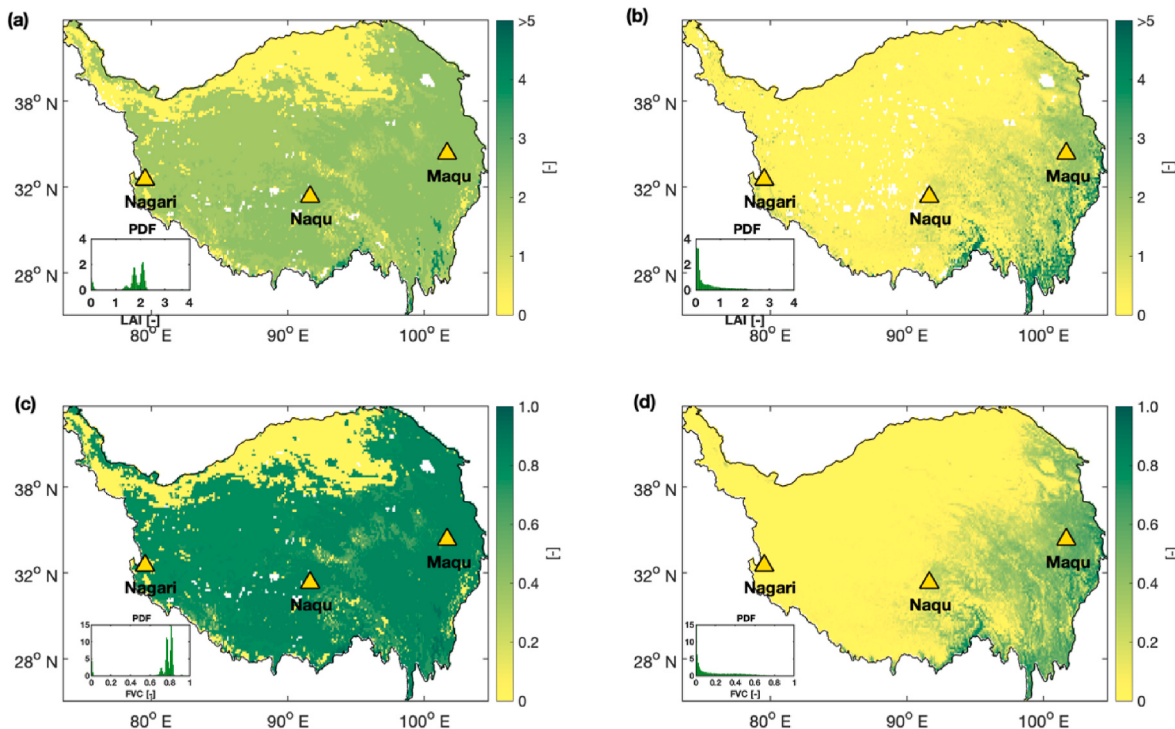


Fig. 3. JJA averaged distribution of LUT-based LAI (a) and FVC (c), and satellite observed LAI (b) and FVC (d) in year 2010. Insets denote Probability Density Function (PDF) of analyzed variables. Triangles indicate the locations of three soil temperature in-situ observations.

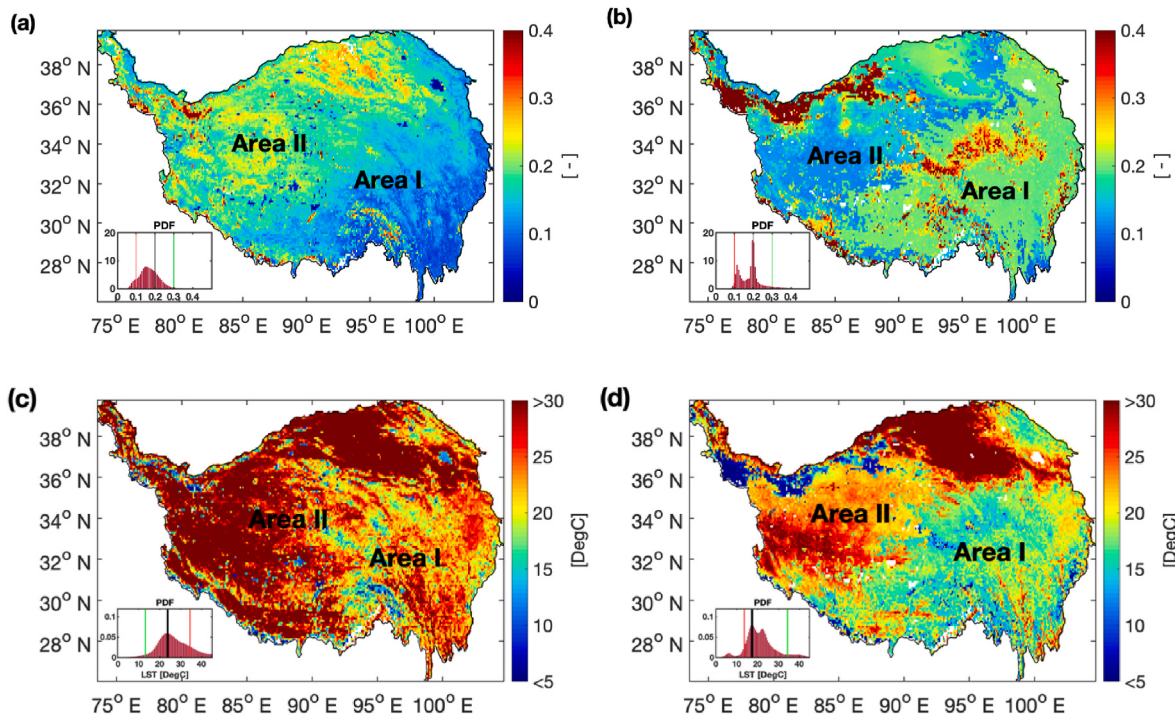


Fig. 4. JJA averaged distribution of satellite-observed albedo (a) and LST (c), and LUT-based albedo (b) and LST (d) in year 2010. Insets denote Probability Density Function (PDF) of analyzed variables. Black, red and green solid lines indicate variables at maximum, 50 and 25 percentiles of their probability density, respectively. (For interpretation of the references to color in this figure legend, the reader is referred to the Web version of this article.)

higher values (positive biases) in the more vegetated southeastern part whereas lower (negative biases) in the Northwest. Such contrast between satellite and CTL experiment can also be reflected in the probability distribution of the albedo, e.g., the probability density distribution satellite albedo is unimodal while the result from CTL experiment is

bimodally distributed. The bias of albedo is then transferred to the LST simulation in the CTL experiment. Fig. 4c and d shows that compared to the satellite observed LST, the CTL experiment shows overall cold biases over the study region. The probability density distribution of satellite LST is warmly skewed, with more than 90% of grids located above 20 °C

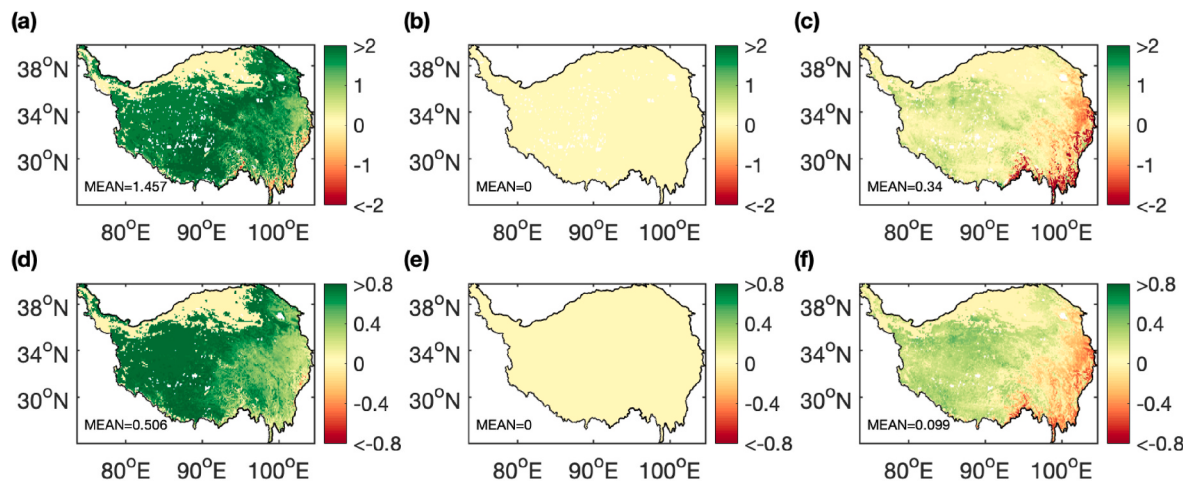


Fig. 5. Difference map of LAI (top) and FVC (bottom) between three experiments and satellite observations. Three experiments are Exp_CTL (left), Exp_RS (middle) and Exp_RL02 (right), respectively. Blank areas indicate missing values.

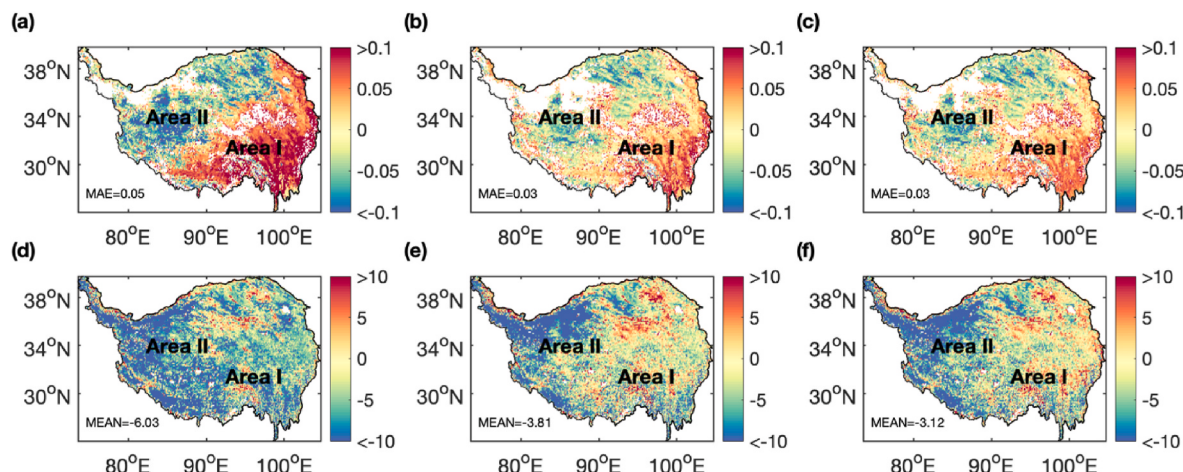


Fig. 6. Difference map of albedo (top) and LST (bottom) between three experiments and satellite observations. Three experiments are the experiment CTL (left), experiment RS (middle) and experiment RL02 (right), respectively. Areas with albedo larger than 0.35 are masked to exclude the snowing effects. Blank areas indicate missing values.

(degC) whereas the number of grids is only 55% in CTL experiment. The bimodal spatial distribution of LST is also presented in the CTL experiment – the southeastern area shows generally cold temperature with LST

below 20 degC whereas in the northwestern part LST is consistently larger than 25 degC.

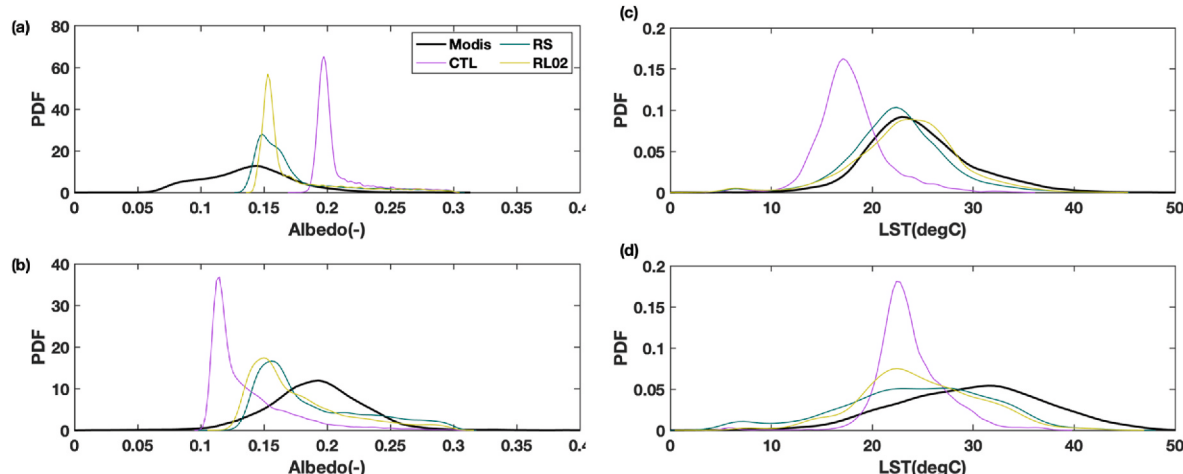


Fig. 7. Probability Density Function (PDF, unitless) of albedo (a and b) and LST (c and d) over two subregions: a and c for Area I, b and d for Area II.

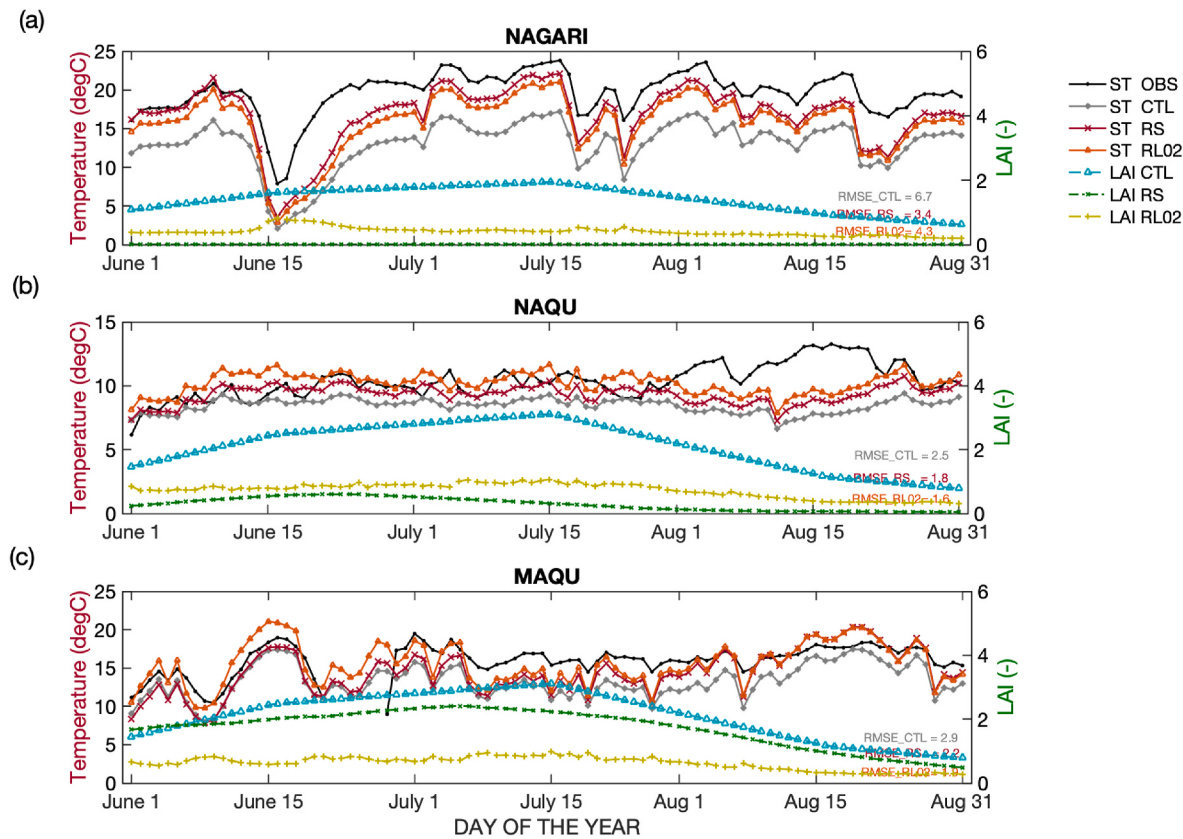


Fig. 8. Surface soil temperature (0–5 cm) results at three in-situ stations: (a) Nagari; (b) Naqu; and (c) Maqu. Black solid line with dot markers denotes in-situ observations. Solid lines with gray, crimson and orange colors denote soil temperature from the CTL experiment, RS experiment and RL02 experiment, respectively. Dash lines with cyan, green and yellow-green denote LAI time series from the three experiments. (For interpretation of the references to color in this figure legend, the reader is referred to the Web version of this article.)

3.3. Results from RS and RL02 experiments

Fig. 5 shows the inter-comparison of LAI and FVC in three experiments compared with satellite observations. Compared to the overestimation in the CTL experiment, LAI and FVC in experiment RS and experiment RL02 are notably reduced (Fig. 4, middle and right columns). The mean bias of LAI in the RL02 run is 0.34 compared to 1.46 in the CTL experiment; the mean bias for FVC is 0.10 relative to 0.50. The biases in the experiment RS are zero since in this case the remote sensing LAI and FVC are directly incorporated as input to the model runs. In terms of the spatial pattern, the overestimation of LAI and FVC in the CTL experiment is more noticeable in the northwestern areas, showing similar dependence on vegetation types. Analogous distribution is also observed in the experiment RL02, although it is worth noting that the LAI and FVC in the southeastern area are underestimated compared to the satellite observations (see Fig. 5).

The spatial distribution of albedo and LST simulation differences between the three experiments and MODIS observations are shown in Fig. 6. Overall, the albedo from experiment RS and RL02 compares much closer to the satellite observations than experiment CTL. Even though the mean bias of albedo simulation is not improved substantially (e.g., from 0.03 to 0.02) – because the positive bias in Area I cancel out with the negative bias over Area II – the difference between the simulated albedo and satellite observation is noticeably lower in each region. Cold biases of LST simulations are also improved in experiments RS and RL02 – the LST mean bias is reduced by 2.2 degC and 2.9 degC in each experiment and RMSE is reduced by 1.5 degC in both model runs.

Fig. 7 shows the probability density distribution of albedo and LST in the three experiments over the two divided regions with primary vegetation types (e.g., Area I and Area II in Fig. 1) respectively. In Area I

where the land is covered by dense vegetation, the probability density of albedo in the CTL experiment is highly right-skewed (Fig. 7a, magenta line), whereas in experiments RS and RL02, the curves are symmetrically distributed, centered around 0.15 (Fig. 7a, green and yellow lines). The PDF curves from three experiments in Area II show consistent unsymmetrical distribution, although the RS and RL02 curves compare closer to the MODIS distribution (Fig. 7b). The LST statistics show much the same behaviors. The dependence of albedo and LST on vegetation types can be explained by the dependence of Noah-MP's energy transfer scheme on plant trait parameters (e.g., parameters in Table 1).

3.4. Validation using in-situ observations

The simulated surface soil temperature (ST) results are then validated by in-situ observations in Fig. 8. Overall, the temporal variability of ST from the three experiments compares reasonably to the observations at the three sites, except that at the Naqu station, the three experiments all failed in simulating the late-summer peak (Fig. 8b). However, the three experiments show divergent behaviors in terms of the mean value, in which the experiment CTL shows significant cold biases compared to the other two experiments. Compared to the in-situ observation, the cold biases of ST in the CTL experiment are particularly large at the Nagari station, showing an RMSE of 6.7 degC. By comparison, the ST simulations in experiments RS and RL02 compare closer to the in-situ measurements, with RMSE reduced by larger than 20% at each site.

The LAI time series in all experiments also show consistent temporal variations with the observation of peaks in the midsummer (Fig. 8, dash lines). However, they do not show as much seasonal variability as the ST results, except for the LAI series in the RL02 experiment at the Maqu

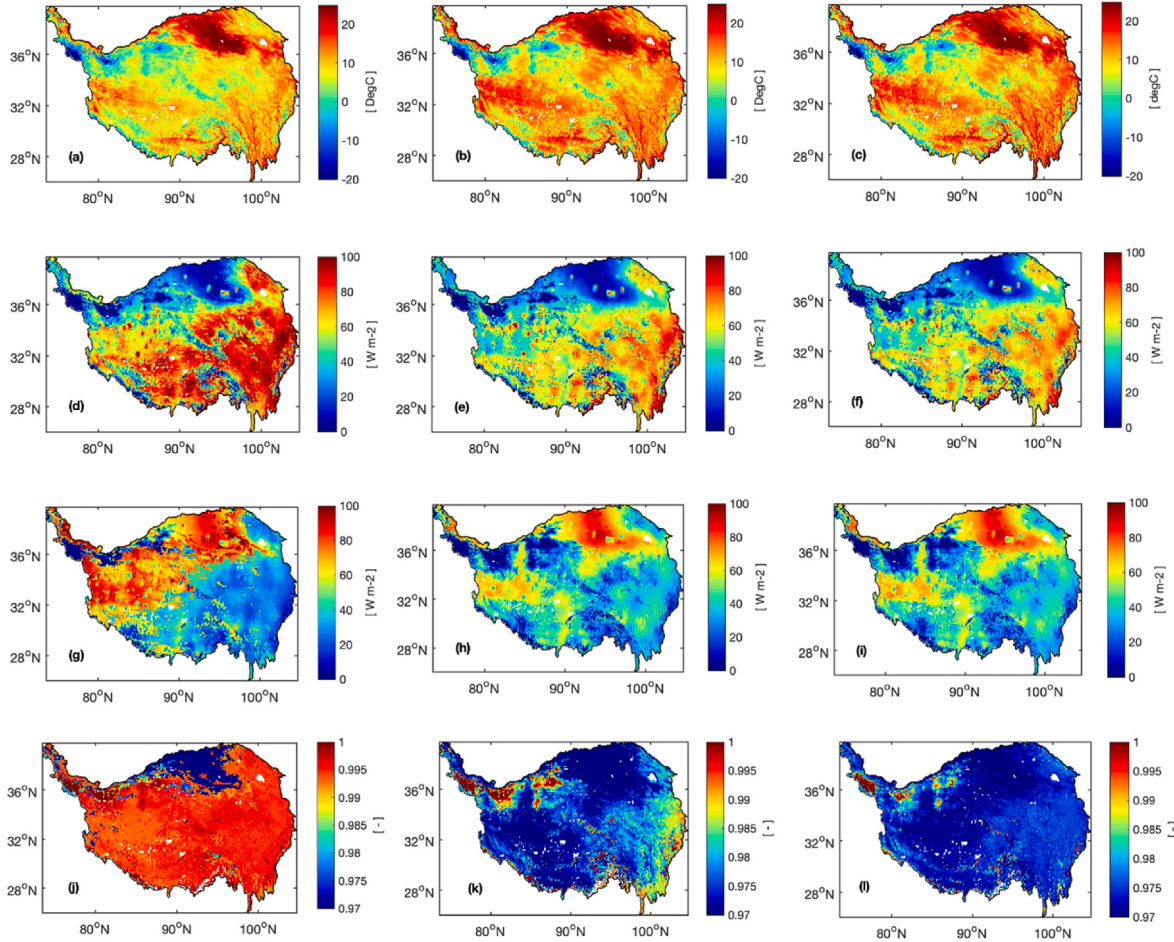


Fig. 9. Simulated surface soil temperature (a–c), latent heat flux (d–f), sensible heat flux (g–l), and surface longwave emissivity (j–l) from exp_CTL (left column), exp_RS (middle column), and exp_RL02 (right column).

station. LAI in the experiment CTL is substantially overestimated at three sites when compared to the observation, corresponding to the cold bias of its ST time series. Incorporating satellite observed vegetation parameters (i.e., LAI, FVEG in experiment RS and CI in experiment RL02) effectively reduces the overestimation of LAI and thus the cold bias in the ST simulations. The substantial cut-down of LAI still has impacts on the ST in amplitude.

The improvement of ST simulations is dependent on the vegetation conditions. Stations with less covered vegetation (i.e., Nagari) show more significant ST improvement than stations with more densely covered vegetation (i.e., Maqu and Naqu) (Fig. 8b and c). These results suggest that in addition to vegetation types, the energy transfer process in Noah-MP also depends on the vegetation coverage. These results are consistent with Lorenz et al. (2013), who suggest that the phenology of vegetation does not directly influence the evolution of surface temperature but rather its magnitude, especially in areas with low interannual LAI variability.

3.5. Comparison of energy budget related variables

To understand how vegetation changes help improve the model's land surface temperature simulations, we further analyzed four energy budget variables, i.e., surface soil temperature, latent and sensible heat fluxes, and surface longwave emissivity from the three experiments. The results are shown in Fig. 9. In exp_CTL, the surface longwave emissivity is higher than 0.99 all over the study region (except for Qaidam desert, where the emissivity is approximately 0.97). The high surface emissivity causes more energy loss through sensible (higher in the northwestern

and inland areas) and latent heat fluxes (higher in the southeastern areas). Compared to exp_CTL, the surface longwave emissivity in exp_RS and exp_RL02 is significantly reduced (e.g., from 0.99 to lower than 0.97; more substantial in exp_RL02). Correspondingly, the heat fluxes in both experiments also decrease, leading to higher surface soil temperature. The intercomparisons among experiments here reflect the model's energy transfer chain and further highlight that LAI and FVC do play important roles in regulating energy budget and their representations should be treated appropriately in LSMs.

4. Discussion and conclusions

This study set out to improve the LST simulations in the Noah-MP land surface model by improving the model's vegetation parameters (i.e., LAI and FVC) on the Tibetan Plateau. LAI and FVC from remote sensing products and an empirical LAI and FVC scheme are implemented. The resulting simulations are then compared with satellite observations and validated by in-situ observations. We show that the prescribed LAI and FVC in Noah-MP (i.e., LUT and parameterization-based) are largely overestimated compared to the satellite observations. The overestimation of LAI and FVC then leads to large cold biases of the model's LST simulation. Using satellite LAI and FVC products, the model's LST simulation as well as other surface energy balance related variables (e.g., albedo) are considerably improved, the degree of which is comparable to the improvement using the parameterization-based method. However, the LST improvements using both methods are more significant over the areas that are densely covered (Area I). The LST simulation in bare soil areas (Area II) still shows large biases.

One limitation of this study is that even though remote sensing products provide large-scale observations, such datasets often contain uncertainties, which may propagate to other variables through water and energy cycles in land surface model. To quantify this, we have conducted synthetic analyses on the sensitivity of the model's energy transfer process to LAI and FVC variability. Here we chose surface albedo as an example variable in the model's energy transfer process since the albedo algorithm is less complicated and therefore more feasible for replication compared to other variables. The sensitivity function here is consistent to albedo calculation algorithm in Noah-MP. From the results it can be seen that the albedo sensitivity to LAI and FVC input is dependent on vegetation types (Fig. S3). The albedo is more sensitive to LAI and FVC changes over grassland-covered areas, but much less insensitive over forest and shrubland covered areas. This means the model simulation in Area-I contains larger uncertainty yielding from remote sensing products. However, the uncertainty will not be that large since the bias range of GLASS LAI and FVC product (represented by RMSE) is limited within 0.8 (Ma and Liang, 2022), and 0.25 (Xiao et al. 2016), respectively. Linking this with Fig. S4, the simulated albedo uncertainty from remote sensing products is at most 0.05, which is relatively minor. The above analyses indicate that even though the LAI and FVC uncertainty exist and cannot be avoided, the simulated albedo will not be biased dramatically over Tibetan Plateau, where the vegetation types are mainly grasslands and mixed grasslands.

Our method resembles one previous study (Li et al. (2019)) in that we both use satellite LAI and FVC products to improve LST simulation in LSMs. The main difference is that the LSM in Li et al. (2019) is the Common Land Model (CoLM) instead of the Noah-MP we employ here. In fact, the LST improvement in Li et al. (2019) is more significant than ours since the original LAI and FVC scheme is more fixed in CoLM (e.g., its LAI LUT does not have seasonal variations, and the FVC is prescribed as a binary variable at each grid cell). Therefore, the results in this study partially demonstrate that the vegetation schemes for land surface energy balance simulation in Noah-MP are overall more reasonable than those in CoLM. But still, our result here proves that over the densely vegetation covered area, there is space for improvement in LST simulation using the original Noah-MP scheme, and such shortcomings can be mended by incorporating the remote sensing LAI and FVC products. For the area with sparse vegetation cover or mostly bare soils (e.g., Area II), since the land surface energy balance is dominated by soil parameters, further improvement can be achieved through modifications on soil roughness schemes. A relevant analysis has already been conducted in Noah LSM and proved effective in improving LST simulations over these areas on Tibetan Plateau (Chen et al., 2011).

Finally, we should point out that although the methodology in current manuscript - that is, using satellite LAI and FVC images to improve LSMs – is as previously discussed, not the first time applied for the land surface models. However, application of such a method is still beneficial for the development of Noah-MP LSM itself, especially for the regions of Tibetan Plateau where LSMs are not well calibrated. Our results show that incorporation of remote sensing vegetation products can improve the model's LST as well as other energy budget component in an equivalent degree to parameterization scheme-based improvement. Therefore, the results further highlight the feasibility and benefit of incorporating remote sensing data in facilitating land surface model development. Moreover, the methodology in this study is of substantial simplicity compared to other remote sensing-based approach, e.g., data assimilation (Ling et al., 2019; Ling et al., 2019), which will sufficiently improve the computing efficiency.

Declaration of competing interest

The authors declare that they have no known competing financial interests or personal relationships that could have appeared to influence the work reported in this paper.

Data availability

Data will be made available on request.

Acknowledgements

This work was jointly supported by the Second Tibetan Plateau Scientific Expedition and Research Program (STEP, grant No. 2019QZKK0206), the National Key Research and Development Program of China (2022YFC3002901), and the International Partnership Program of Chinese Academy of Sciences (Grant No. 183311KYSB20200015).

Appendix A. Supplementary data

Supplementary data to this article can be found online at <https://doi.org/10.1016/j.srs.2023.100115>.

References

- Barlage, M., Tewari, M., Chen, F., Miguez-Macho, G., Yang, Z.-L., Niu, G.-Y., 2015. The effect of groundwater interaction in North American regional climate simulations with WRF/Noah-MP. *Climatic Change* 129, 485–498. <https://doi.org/10.1007/s10584-014-1308-8>.
- Cai, X., Yang, Z.-L., David, C.H., Niu, G.-Y., Rodell, M., 2014a. Hydrological evaluation of the Noah-MP land surface model for the Mississippi River Basin: hydrological evaluation of noah-mp. *J. Geophys. Res. Atmos.* 119, 23–38. <https://doi.org/10.1002/2013JD020792>.
- Cai, X., Yang, Z.-L., Xia, Y., Huang, M., Wei, H., Leung, L.R., Ek, M.B., 2014b. Assessment of simulated water balance from Noah, Noah-MP, CLM, and VIC over CONUS using the NLDAS test bed. *J. Geophys. Res. Atmos.* 119, 13,751–13,770. <https://doi.org/10.1002/2014JD022113>.
- Camacho, F., Cernicharo, J., Lacaze, R., Baret, F., Weiss, M., 2013. GEOV1: LAI, FAPAR essential climate variables and FCOVER global time series capitalizing over existing products. Part 2: validation and intercomparison with reference products. *Rem. Sens. Environ.* 137, 310–329. <https://doi.org/10.1016/j.rse.2013.02.030>.
- Chen, J.M., Liu, J., Leblanc, S.G., Lacaze, R., Roujean, J.-L., 2003. Multi-angular optical remote sensing for assessing vegetation structure and carbon absorption. *Rem. Sens. Environ.* 84, 516–525. [https://doi.org/10.1016/S0034-4257\(02\)00150-5](https://doi.org/10.1016/S0034-4257(02)00150-5).
- Chen, Y., Yang, K., He, J., Qin, J., Shi, J., Du, J., He, Q., 2011. Improving land surface temperature modeling for dry land of China. *J. Geophys. Res.* 116, D20104 <https://doi.org/10.1029/2011JD015921>.
- Dai, Y., Zeng, X., Dickinson, R.E., Baker, I., Bonan, G.B., Bosilovich, M.G., Denning, A.S., Dirmeyer, P.A., Houser, P.R., Niu, G., Oleson, K.W., Schlosser, C.A., Yang, Z.-L., 2003. The Common land model. *Bull. Am. Meteorol. Soc.* 84, 1013–1024. <https://doi.org/10.1175/BAMS-84-8-1013>.
- Dickinson, R.E., 1983. Land surface processes and climate—surface lbedos and energy balance. In: Advances in Geophysics. Elsevier, pp. 305–353. [https://doi.org/10.1016/S0065-2687\(08\)60176-4](https://doi.org/10.1016/S0065-2687(08)60176-4).
- Gao, Y., Xu, J., Chen, D., 2015. Evaluation of WRF mesoscale climate simulations over the Tibetan plateau during 1979–2011. *J. Clim.* 28, 2823–2841. <https://doi.org/10.1175/JCLI-D-14-00300.1>.
- García-García, A., Cuesta-Valero, F.J., Beltrami, H., González-Rouco, J.F., García-Bustamante, E., Finniss, J., 2020. Land Surface Model influence on the simulated climatologies of temperature and precipitation extremes in the WRF v.3.9 model over North America (preprint). *Atmospheric Sciences*. <https://doi.org/10.5194/gmd-2020-86>.
- Garrigues, S., Lacaze, R., Baret, F., Morisette, J.T., Weiss, M., Nickeson, J.E., Fernandes, R., Plummer, S., Shabanov, N.V., Myneni, R.B., Knyazikhin, Y., Yang, W., 2008. Validation and intercomparison of global Leaf Area Index products derived from remote sensing data: global LAI products intercomparison. *J. Geophys. Res.* 113 <https://doi.org/10.1029/2007JG000635> n/a-n/a.
- Gentine, P., Entekhabi, D., Polcher, J., 2011. The diurnal behavior of evaporative fraction in the soil–vegetation–atmospheric boundary layer continuum. *J. Hydrometeorol.* 12, 1530–1546. <https://doi.org/10.1175/2011JHM1261.1>.
- Gentine, P., Holtlag, A.A.M., D'Andrea, F., Ek, M., 2013. Surface and atmospheric controls on the onset of moist convection over land. *J. Hydrometeorol.* 14, 1443–1462. <https://doi.org/10.1175/JHM-D-12-0137.1>.
- Guo, D., Wang, H., 2013. Simulation of permafrost and seasonally frozen ground conditions on the Tibetan Plateau, 1981–2010: change in frozen ground. *J. Geophys. Res. Atmos.* 118, 5216–5230. <https://doi.org/10.1002/jgrd.50457>.
- He, J., Yang, K., Tang, W., Lu, H., Qin, J., Chen, Y., Li, X., 2020. The first high-resolution meteorological forcing dataset for land process studies over China. *Sci. Data* 7, 25. <https://doi.org/10.1038/s41597-020-0369-y>.
- He, L., Chen, J.M., Pisek, J., Schaaf, C.B., Strahler, A.H., 2012. Global clumping index map derived from the MODIS BRDF product. *Rem. Sens. Environ.* 119, 118–130. <https://doi.org/10.1016/j.rse.2011.12.008>.
- Jarvis, P.G., 1976. The interpretation of the variations in leaf water potential and stomatal conductance found in canopies in the field. *Philos. Trans. R. Soc. B* 273, 593–610. <https://doi.org/10.1098/rstb.1976.0035>.

- Ji, D., Dai, Y.-J., 2010. The Common Land Model (CoLM) Technical Guide.
- Jiao, Z., Dong, Y., Schaaf, C.B., Chen, J.M., Román, M., Wang, Z., Zhang, H., Ding, A., Erb, A., Hill, M.J., Zhang, X., Strahler, A., 2018. An algorithm for the retrieval of the clumping index (CI) from the MODIS BRDF product using an adjusted version of the kernel-driven BRDF model. *Rem. Sens. Environ.* 209, 594–611. <https://doi.org/10.1016/j.rse.2018.02.041>.
- Kang, Z., Qiu, B., Xiang, Z., Liu, Y., Lin, Z., Guo, W., 2022. Improving simulations of vegetation dynamics over the Tibetan plateau: role of atmospheric forcing data and spatial resolution. *Adv. Atmos. Sci.* 39, 1115–1132. <https://doi.org/10.1007/s00376-022-1426-6>.
- Kumar, S.V., Mocko, M., D., Wang, S., Peters-Lidard, C.D., Borak, J., 2019. Assimilation of remotely sensed leaf area index into the noah-MP land surface model: impacts on water and carbon fluxes and states over the continental United States. *J. Hydrometeorol.* 20, 1359–1377. <https://doi.org/10.1175/JHM-D-18-0237.1>.
- Lawrence, D.M., Oleson, K.W., Flanner, M.G., Thornton, P.E., Swenson, S.C., Lawrence, P.J., Zeng, X., Yang, Z.-L., Levis, S., Sakaguchi, K., Bonan, G.B., Slater, A.G., 2011. Parameterization improvements and functional and structural advances in version 4 of the community land model. *J. Adv. Model. Earth Syst.* 3, M03001 <https://doi.org/10.1029/2011MS00045>.
- Li, C., Lu, H., Leung, L.R., Yang, K., Li, H., Wang, W., Han, M., Chen, Y., 2019. Improving land surface temperature simulation in CoLM over the Tibetan plateau through fractional vegetation cover derived from a remotely sensed clumping index and model-simulated leaf area index. *J. Geophys. Res. Atmos.* 124, 2620–2642. <https://doi.org/10.1029/2018JD028640>.
- Li, Xin, Che, T., Li, Xinwu, Wang, L., Duan, A., Shangguan, D., Pan, X., Fang, M., Bao, Q., 2020. CASEarth Poles: big data for the three Poles. *Bull. Am. Meteorol. Soc.* 101, E1475–E1491. <https://doi.org/10.1175/BAMS-D-19-0280.1>.
- Liang, J., Yang, Z., Lin, P., 2019. Systematic hydrological evaluation of the noah-MP land surface model over China. *Adv. Atmos. Sci.* 36, 1171–1187. <https://doi.org/10.1007/s00376-019-9016-y>.
- Ling, X.L., Fu, C.B., Yang, Z.L., Guo, W.D., 2019a. Comparison of different sequential assimilation algorithms for satellite-derived leaf area index using the Data Assimilation Research Testbed (version Lanai). *Geosci. Model Dev. (GMD)* 12, 3119–3133. <https://doi.org/10.5194/gmd-12-3119-2019>.
- Ling, X.L., Fu, C.B., Guo, W.D., Yang, Z.L., 2019b. Assimilation of remotely sensed LAI into CLM4CN using DART. *JAdv Model Earth Sy* 11, 2768–2786. <https://doi.org/10.1029/2019ms001634>.
- Liu, J.-G., Xie, Z.-H., 2013. Improving simulation of soil moisture in China using a multiple meteorological forcing ensemble approach. *Hydrol. Earth Syst. Sci.* 17, 3355–3369. <https://doi.org/10.5194/hess-17-3355-2013>.
- Liu, Y., Xiao, J., Ju, W., Zhu, G., Wu, X., Fan, W., Li, D., Zhou, Y., 2018. Satellite-derived LAI products exhibit large discrepancies and can lead to substantial uncertainty in simulated carbon and water fluxes. *Rem. Sens. Environ.* 206, 174–188. <https://doi.org/10.1016/j.rse.2017.12.024>.
- Lorenz, R., Davin, E.L., Lawrence, D.M., Stöckli, R., Seneviratne, S.I., 2013. How important is vegetation phenology for European climate and heat waves? *J. Clim.* 26, 10077–10100. <https://doi.org/10.1175/JCLI-D-13-00040.1>.
- Ma, H., Liang, S., 2022. Development of the GLASS 250-m leaf area index product (version 6) from MODIS data using the bidirectional LSTM deep learning model. *Rem. Sens. Environ.* 273, 112985 <https://doi.org/10.1016/j.rse.2022.112985>.
- Ma, N., Niu, G.-Y., Xia, Y., Cai, X., Zhang, Y., Ma, Y., Fang, Y., 2017. A systematic evaluation of noah-MP in simulating land-atmosphere energy, water, and carbon exchanges over the continental United States: noah-MP evaluation in CONUS. *J. Geophys. Res. Atmos.* 122, 12,245–12,268. <https://doi.org/10.1002/2017JD027597>.
- Niu, J., 2000. A simulation of biomes on the Tibetan plateau and their responses to global climate change. *Mt. Res. Dev.* 20, 80–89. [https://doi.org/10.1659/0276-4741\(2000\)020\[0080:ASBOT\]2.0.CO;2](https://doi.org/10.1659/0276-4741(2000)020[0080:ASBOT]2.0.CO;2).
- Niu, G.-Y., Yang, Z.-L., Mitchell, K.E., Chen, F., Ek, M.B., Barlage, M., Kumar, A., Manning, K., Niyogi, D., Rosero, E., Tewari, M., Xia, Y., 2011. The community Noah land surface model with multiparameterization options (Noah-MP): 1. Model description and evaluation with local-scale measurements. *J. Geophys. Res.* 116, D12109 <https://doi.org/10.1029/2010JD015139>.
- Nogueira, M., Albergel, C., Boussetta, S., Johannsen, F., Trigo, I.F., Ermida, S.L., Martins, J.P.A., Dutra, E., 2020. Role of vegetation in representing land surface temperature in the CHTESSEL (CY45R1) and SURFEX-ISBA (v8.1) land surface models: a case study over Iberia (preprint). Climate and Earth System Modeling. <https://doi.org/10.5194/gmd-2020-49>.
- Roujean, J.-L., 1996. A tractable physical model of shortwave radiation interception by vegetative canopies. *J. Geophys. Res.* 101, 9523–9532. <https://doi.org/10.1029/96JD00043>.
- Roujean, J.-L., Lacaze, R., 2002. Global mapping of vegetation parameters from POLDER multiangular measurements for studies of surface-atmosphere interactions: a pragmatic method and its validation. *J. Geophys. Res.* 107, 4150. <https://doi.org/10.1029/2001JD000751>.
- Sakaguchi, K., Zeng, X., 2009. Effects of soil wetness, plant litter, and under-canopy atmospheric stability on ground evaporation in the Community Land Model (CLM3.5): new schemes for CLM3.5 soil evaporation. *J. Geophys. Res.* 114 <https://doi.org/10.1029/2008JD010834>.
- Scurlock, J.M.O., Asner, G.P., Gower, 2002. Worldwide Historical Estimates of Leaf Area Index, 1932–2000. U.S. Department of Energy (DOE).
- Sellers, P.J., 1985. Canopy reflectance, photosynthesis and transpiration. *Int. J. Rem. Sens.* 6, 1335–1372. <https://doi.org/10.1080/01431168508948283>.
- Sellers, P.J., Randall, D.A., Collatz, G.J., Berry, J.A., Field, C.B., Dazlich, D.A., Zhang, C., Collelo, G.D., Bounoua, L., 1996. A revised land surface parameterization (SiB2) for atmospheric GCMS. Part I: model formulation. *J. Clim.* 9, 676–705.
- Seneviratne, S.I., Corti, T., Davin, E.L., Hirschi, M., Jaeger, E.B., Lehner, I., Orlowsky, B., Teuling, A.J., 2010. Investigating soil moisture–climate interactions in a changing climate: a review. *Earth Sci. Rev.* 99, 125–161. <https://doi.org/10.1016/j.earscirev.2010.02.004>.
- Su, Z., Wen, J., Dente, L., van der Velde, R., Wang, L., Ma, Y., Yang, K., Hu, Z., 2011. The Tibetan Plateau observatory of plateau scale soil moisture and soil temperature (Tibet-Obs) for quantifying uncertainties in coarse resolution satellite and model products. *Hydrol. Earth Syst. Sci.* 15, 2303–2316. <https://doi.org/10.5194/hess-15-2303-2011>.
- Sun, J., Chen, Y., Yang, K., Lu, H., Zhao, L., Zheng, D., 2021. Influence of organic matter on soil hydrothermal processes in the Tibetan Plateau: observation and parameterization. *J. Hydrometeorol.* <https://doi.org/10.1175/JHM-D-21-0059.1>.
- Sun, S., Zheng, D., Liu, S., Xu, Z., Xu, T., Zheng, H., Yang, X., 2022. Assessment and improvement of Noah-MP for simulating water and heat exchange over alpine grassland in growing season. *Sci. China Earth Sci.* 65, 536–552. <https://doi.org/10.1007/s11430-021-9852-2>.
- Tian, L., Jin, J., Wu, P., Niu, G., Zhao, C., 2020. High-resolution simulations of mean and extreme precipitation with WRF for the soil-erosive Loess Plateau. *Clim. Dynam.* 54, 3489–3506. <https://doi.org/10.1007/s00382-020-05178-6>.
- Vergeghy, D.L., 1991. CLASS-A Canadian land surface scheme for GCMS: I. Soil model. *Int. J. Climatol.* 11, 111–133. <https://doi.org/10.1002/joc.3370110202>.
- Wan, Z., 2013. Collection-6 MODIS Land Surface Temperature Products Users' Guide.
- Wang, A., Barlage, M., Zeng, X., Draper, C.S., 2014. Comparison of land skin temperature from a land model, remote sensing, and in situ measurement: comparison of land skin temperature. *J. Geophys. Res. Atmos.* 119, 3093–3106. <https://doi.org/10.1002/2013JD021026>.
- Wang, W., Yang, K., Zhao, Long, Zheng, Z., Lu, H., Mamtimin, A., Ding, B., Li, X., Zhao, Lin, Li, H., Che, T., Moore, J.C., 2020. Characterizing surface albedo of shallow fresh snow and its importance for snow ablation on the interior of the Tibetan plateau. *J. Hydrometeorol.* 21, 815–827. <https://doi.org/10.1175/JHM-D-19-0193.1>.
- Xiao, Z., Liang, S., Wang, J., Chen, P., Yin, X., Zhang, L., Song, J., 2014. Use of general regression neural networks for generating the GLASS leaf area index product from time-series MODIS surface reflectance. *IEEE Trans. Geosci. Rem. Sens.* 52, 209–223. <https://doi.org/10.1109/TGRS.2013.2237780>.
- Xiao, Z., Liang, S., Wang, J., Xiang, Y., Zhao, X., Song, J., 2016a. Long-time-series global land surface satellite leaf area index product derived from MODIS and AVHRR surface reflectance. *IEEE Trans. Geosci. Rem. Sens.* 54, 5301–5318. <https://doi.org/10.1109/TGRS.2016.2560522>.
- Xiao, Z., Wang, T., Liang, S., Sun, R., 2016b. Estimating the fractional vegetation cover from GLASS leaf area index product. *Rem. Sens.* 8, 337. <https://doi.org/10.3390/rs8040337>.
- Yang, F., Lu, H., Yang, K., He, J., Wang, W., Wright, J.S., Li, C., Han, M., Li, Y., 2017. Evaluation of multiple forcing data sets for precipitation and shortwave radiation over major land areas of China. *Hydrol. Earth Syst. Sci.* 21, 5805–5821. <https://doi.org/10.5194/hess-21-5805-2017>.
- Yang, K., Chen, Y., He, J., Zhao, L., Lu, H., Qin, J., Zheng, D., Li, X., 2020. Development of a daily soil moisture product for the period of 2002–2011 in Chinese mainland. *Sci. China Earth Sci.* 63, 1113–1125. <https://doi.org/10.1007/s11430-019-9588-5>.
- Yang, K., Chen, Y.-Y., Qin, J., 2009. Some practical notes on the land surface modeling in the Tibetan Plateau. *Hydrol. Earth Syst. Sci.* 13, 687–701. <https://doi.org/10.5194/hess-13-687-2009>.
- Yang, R., Friedl, M.A., 2003. Modeling the effects of three-dimensional vegetation structure on surface radiation and energy balance in boreal forests. *J. Geophys. Res.* 108 (D16), 8615. <https://doi.org/10.1029/2002JD003109>.
- Yang, Z.-L., Niu, G.-Y., 2003. The versatile integrator of surface and atmosphere processes. *Global Planet. Change* 38, 175–189. [https://doi.org/10.1016/S0921-8181\(03\)00028-6](https://doi.org/10.1016/S0921-8181(03)00028-6).
- Yang, Z.-L., Niu, G.-Y., Mitchell, K.E., Chen, F., Ek, M.B., Barlage, M., Longuevergne, L., Manning, K., Niyogi, D., Tewari, M., Xia, Y., 2011. The community Noah land surface model with multiparameterization options (Noah-MP): 2. Evaluation over global river basins. *J. Geophys. Res.* 116, D12109 <https://doi.org/10.1029/2010JD015139>.
- Zheng, D., van der Velde, R., Su, Z., Wang, X., Wen, J., Booij, M.J., Hoekstra, A.Y., Chen, Y., 2015. Augmentations to the Noah model physics for application to the yellow river source area. Part II: turbulent heat fluxes and soil heat transport. *J. Hydrometeorol.* 16, 2677–2694. <https://doi.org/10.1175/JHM-D-14-0199.1>.
- Zhu, G., 2016. Spatial-temporal characteristics of foliage clumping index in China during 2000–2013. *Chin. Sci. Bull.* 61, 1595–1603. <https://doi.org/10.1360/N972015-00987>.
- Zhu, G., Ju, W., Chen, J.M., Gong, P., Xing, B., Zhu, J., 2012. Foliage clumping index over China's landmass retrieved from the MODIS BRDF parameters product. *IEEE Trans. Geosci. Rem. Sens.* 50, 2122–2137. <https://doi.org/10.1109/TGRS.2011.2172213>.